On the Kite-Platform Interactions in Offshore Airborne Wind Energy Systems: Frequency Analysis and Control Approach

Sofia Trombini, Edoardo Pasta, Lorenzo Fagiano

Abstract— This study investigates deep offshore, pumping Airborne Wind Energy systems, focusing on the kite-platform interaction. The considered system includes a 360 m^2 soft-wing kite, connected by a tether to a winch installed on a 10-meter-deep spar with four mooring lines. Wind power is converted into electricity with a feedback controlled periodic trajectory of the kite and corresponding reeling motion of the tether. An analysis of the mutual influence between the platform and the kite dynamics, with different wave regimes, reveals a rather small sensitivity of the flight pattern to the platform oscillations; on the other hand, the frequency of tether force oscillations can be close to the platform resonance peaks, resulting in possible increased fatigue loads and damage of the floating and submerged components. A control design procedure is then proposed to avoid this problem, acting on the kite path planner. Simulation results confirm the effectiveness of the approach.

I. INTRODUCTION

Airborne Wind Energy Systems (AWES) convert high-altitude wind energy using a tethered aircraft, or kite [1]. AWES can reach altitudes higher than 300 m above ground, where winds are strong with high probability, yielding large capacity factors [2]. Moreover, they can be manufactured, transported and installed at low cost, thanks to the absence of large monolithic components, making them appealing for remote locations. These features make AWES a strong candidate technology to complement traditional wind energy and solar PV and increase the overall penetration of renewables in our energy mix [3]. The main drawback of AWE technologies is the rather high operational complexity, mostly residing in the automation and control system [1].

In the past 20 years, AWES development has significantly increased. Most activities pertain to inland systems, which are more accessible and cheaper for research and development than offshore ones. However, the latter hold the promise of a huge potential impact. In fact, the expected mass of the floating platform for AWES is a rather small fraction than the one required by offshore horizontal-axis wind turbines, thanks to the center of gravity and applied force being close to the sea surface. Moreover, the offshore wind resources are abundant already below 300 m, so that, thanks to the

possibility to harvest energy at different altitude layers (thus limiting the wake interactions), AWES farms can be arranged compactly, reaching a rather high unit density per occupied surface area [4].

Notwithstanding its promising features, there are currently very few contributions in the literature on deep offshore AWES. In [5] and [6], this concept is evaluated using a simplified model. The results indicate technical feasibility, yet considerable platform displacements are observed, while the kite-floater interactions are not treated in detail. Regarding real-world installations, the company Makani Power [7] attempted a medium-scale (500 kW) offshore system deployment in Norway in 2019. Unfortunately, the company operations ended after a few months.

This paper contributes to advance the knowledge on offshore AWES, focusing on the kite-platform interaction. A pumping AWE system is considered, which converts wind power into electricity with a feedback-controlled periodic trajectory of the kite and corresponding reeling motion of the tether. In contrast to [6], the kite model is not mass-less and the tether is a nonlinear spring with elastic constant depending on its length, whereas in [6] it was assumed to be a rigid rod. The first contribution is an analysis of the mutual influence between the platform and the kite dynamics, with different wave regimes, using a 6-degrees-of-freedom (d.o.f.) model of the platform coupled with an established model of the AWE system. We find that the frequency of tether force oscillations can be close to the platform resonance peaks, resulting in possible increased fatigue loads and damage of the floating and submerged components. The second contribution is to propose a control design procedure to avoid this problem, acting on the kite path planner. Simulation results confirm the effectiveness of the approach.

II. SYSTEM DESCRIPTION AND MODEL

We consider a pumping Airborne Wind Energy system installed on a moored spar-buoy, see Fig. 1 for a conceptual layout. We consider a soft kite with one tether, similar to those employed by the company Skysails Power [8], [1], and a simple geometry of the spar-buoy (i.e., a cylinder) partially filled with heavy sand to act as a ballast. The platform is anchored to the seabed with four symmetric catenary moorings.

To model the system, we consider the following four reference frames:

- Fixed, inertial frame (x, y, z), with origin O_W in the platform centre of gravity at rest, i.e. in static equilibrium when no forces other than gravity and buoyancy are

Sofia Trombini and Lorenzo Fagiano are with the Dipartimento di Elettronica, Informazione e Bioingegneria (DEIB), Politecnico di Milano. E-mail addresses: sofia.trombini@polimi.it; lorenzo.fagiano@polimi.it.

Edoardo Pasta is with Marine Offshore Renewable Energy Lab., Dipartimento di Ingegneria Meccanica e Aerospaziale (DIMEAS). E-mail address: edoardo.pasta@polito.it

acting on it. The z-axis points upwards, perpendicular to the sea surface.

- Platform frame (x_P, y_P, z_P) with origin O_P in the platform centre of gravity and axes coinciding at rest with the inertial one.
- AWES platform frame (x_K, y_K, z_K) with origin O_K located at the tether exit point from the platform. At rest, the axes' are parallel to those of the inertial frame.
- AWES local reference system (e_θ, e_ϕ, e_r) with origin O_{KL} in the wing. The unit vectors (e_θ, e_ϕ, e_r) are defined in the fixed reference system (x, y, z) as

$$\begin{bmatrix} e_\theta & e_\phi & e_r \end{bmatrix} =$$
$$\begin{bmatrix} \sin(\theta)\cos(\phi) & -\sin(\phi) & \cos(\theta)\cos(\phi) \\ \sin(\theta)\sin(\phi) & \cos(\phi) & \cos(\theta)\sin(\phi) \\ -\cos(\theta) & 0 & \sin(\theta) \end{bmatrix}$$

where θ and ϕ, named elevation and azimuth, respectively, are the angles describing the wing's position in the inertial frame using polar coordinates (see Fig. 1).

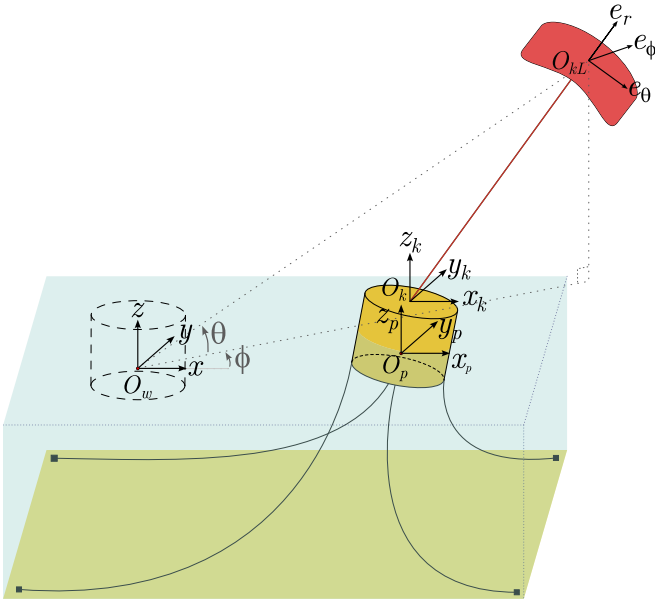The next subsections provide the mathematical equations for each system's component.

Fig. 1: Conceptual layout of the system, with the four considered reference frames.

A. Airborne wind energy system model

We adopt the point-mass AWES model of [9], briefly recalled here for the sake of self-consistency. The kite's position relative to the origin of the inertial reference frame can be expressed using the distance r from O_W to O_{KL} and angles θ and ϕ:

$$\vec{p}_{W-KL}(t) = \begin{bmatrix} r(t)\cos(\theta(t))\cos(\phi(t)) \\ r(t)\cos(\theta(t))\sin(\phi(t)) \\ r(t)\sin(\theta(t)) \end{bmatrix}$$

where $t \in \mathbb{R}$ is the continuous-time variable. Newton's law of motion in the AWES local reference system yields the equations:

$$\ddot{\theta}(t) = \frac{F_\theta(t)}{m(t)\,r(t)}$$
$$\ddot{\phi}(t) = \frac{F_\phi(t)}{m(t)\,r(t)\,\sin(\theta(t))} \qquad (1)$$
$$\ddot{r}(t) = \frac{F_r(t)}{m(t)}$$

where $m(t)$ is the kite's mass m_K augmented by half of the tether mass (see [9]) $m(t) = m_K + \frac{\rho_t \pi d_t^2 L(t)}{8}$ with ρ_t, d_t, and $L(t)$ being, respectively, the tether density, its diameter, and its nominal (i.e., with zero pulling force) length measured from the exit point on the floating platform to the kite. $F_\theta(t)$, $F_\phi(t)$ and $F_r(t)$ in (1) are the resultant forces for each axis of the local reference frame. In particular (variable t is omitted for simplicity): $F_\theta = F_\theta^{grav} + F_\theta^{app} + F_\theta^{aer}$, $F_\phi = F_\phi^{grav} + F_\phi^{app} + F_\phi^{aer}$ and $F_r = F_r^{grav} + F_r^{app} + F_r^{aer} - F^{c,trc}$ where $\vec{F}^{grav}(t)$ is the gravity force, $\vec{F}^{app}(t)$ the apparent force, $\vec{F}^{aer}(t)$ the kite aerodynamic force, and $\vec{F}^{c,trc}(t)$ the tether traction force. The aerodynamic forces are nonlinear functions of the wind speed vector at the kite position, denoted by $\vec{W}(t)$, and depend on the kite effective area A and lift and drag coefficients, C_L, C_D accounting also for the tether drag, which in turn depends on its diameter and length, see e.g. [9] for the details. In this work, the tether is modelled as a nonlinear spring exerting a pulling force equal in absolute value to:

$$F^{c,trc}(t) = \max\left(0, k(L(t))\,\|\vec{P}_{K-KL}(t)\|_2 - L(t)\right) \qquad (2)$$

where $k(L(t))$ is the spring coefficient and $\vec{P}_{K-KL}(t)$ is the vector pointing from O_K to O_{KL}, computed as:

$$\vec{P}_{K-KL}(t) = \vec{P}_{W-KL}(t) - \vec{P}_{W-K}(t), \qquad (3)$$

such that $\|\vec{P}_{K-KL}(t)\|_2$ represents the distance between the kite and the tether exit point on the platform. In (3), $\vec{P}_{W-K}(t)$ is the vector pointing from O_W to O_K, computed as:

$$\vec{P}_{W-K}(t) = \vec{P}_{W-O}(t) + \vec{P}_{O-K} \qquad (4)$$

i.e., the vector sum of $\vec{P}_{W-O}(t)$, pointing from the origin of the inertial plane to the platform's center of gravity, and $\vec{P}_{O-K}$, pointing from the latter to the exit point of the tether. Vector $\vec{P}_{O-K}$ is assumed to be constant, since the platform is modeled as a rigid body, while $\vec{P}_{W-O}(t)$ depends on the position of the platform, as specified later on. About the spring coefficient $k(L(t))$ in (2), this is computed as $k(L(t)) = \frac{\bar{F}^{c,trc}}{\bar{\varepsilon} L(t)}$ where $\bar{F}^{c,trc}$ is the breaking load of the tether, and $\bar{\varepsilon}$ the corresponding elongation (e.g., $\bar{\varepsilon} = 0.03$ means that the tether reaches the breaking load when $\|\vec{P}_{K-KL}(t)\|_2$ equals 1.03 times the nominal tether length, $L(t)$). Regarding the flight control approach, the selected strategy is the one described in [10]. It features a hierarchical structure, where a high-level navigation approach employs two user-defined target points, $P_- = (\theta_-, \phi_-)$ and $P_+ = (\theta_+, \phi_+)$ in the (θ, ϕ) plane, to compute a reference course for the kite at each discrete time step $k \in \mathbb{Z}$ of the digital control loop.

B. Platform model

The motion of objects surrounded by a fluid, like the floating platform considered in this work, is commonly described using the Navier-Stokes' equations [11]. However, their numerical solution is computationally expensive. For this reason, we consider a simplified 6-d.o.f. model based on the linear potential flow theory [12], assuming that the fluid surrounding the body is incompressible and inviscid, and the flow is irrotational [13]. To resolve the dynamics and fulfil boundary requirements on the platform, boundary element techniques (BEMs) are used in conjunction with the linear potential flow theory. In this study, we used the NEMOH programme as a numerical solver to evaluate the hydrodynamic parameters [14].

The platform and its mooring are modeled as a mass-spring-damper system with the addition of specific hydrodynamic forces and moments; the resulting six equations of motion are:

$$M\,\ddot{v}(t) = F^h(t) + F^r(t) + F^{exc}(t) + F^m(t) + F^t(t) \quad (5)$$

where $v(t) = [x_P(t)\ y_P(t)\ z_P(t)\ \omega_{x_P}(t)\ \omega_{y_P}(t)\ \omega_{z_P}(t)]^T$ are the displacements (i.e., surge, sway and heave) and rotations with respect to the platform centre of gravity, $M \in \mathbb{R}^{6\times6}$ is the mass-inertia matrix, vector $F^h \in \mathbb{R}^6$ contains the three-dimensional hydrostatic restoring force and moment, F^r the radiation force and moment, F^{exc} the wave excitation force and moment, F^m the mooring force and moment and F^t the tether traction force and moment applied on the platform.

The hydrostatic restoring effect F^h accounts for the static pressure and gravity force, and it is expressed as $F^h(t) = -K_h v(t)$ where K_h is the restoring coefficient matrix. The radiation force and moment F^r are those exerted by the fluid on the platform when no incident waves are present. Its effect is described as $F^r(t) = -M_\infty \ddot{v}(t) - \int_{-\infty}^t h_{ra}(t-\tau)\dot{v}(\tau)d\tau$ where M_∞ is a 6x6 matrix accounting for the added mass (see [13]), and $h_{ra}(t)$ is the impulse response of the radiation dynamics, which accounts for the memory effect due to the fluid action. The wave excitation F^{exc} accounts for the impact of waves on the platform [13]. Finally, since the mooring lines are modeled as mass-spring-dampers, the mooring force F^m is $F^m(t) = -M_m \ddot{v}(t) - B_m \dot{v}(t) - K_m v(t)$ where M_m is the mooring inertia matrix, B_m is the mooring damping matrix and K_m is the mooring stiffness matrix. These parameters are obtained through a system identification process using data from Orcaflex software. Finally, the tether traction force and moments F^t are computed as:

$$F^t = \begin{bmatrix} \vec{F}^{c,trc} \\ \vec{F}^{c,trc} \times \vec{P}_{O-K} \end{bmatrix} \quad (6)$$

where $\times$ denotes the cross-product, and $\vec{F}^{c,trc} = F^{c,trc}\dfrac{\vec{P}_{K-KL}}{\|\vec{P}_{K-KL}\|_2}$ with $F^{c,trc}$ computed as in (2).

C. Overall model equation

The AWES' and platform's dynamical models are coupled via the tether force (6), which acts on the platform motion (5) and depends on the platform position via the equation $\vec{P}_{W-O}(t) = [x_P(t)\ y_P(t)\ z_P(t)]^T$, see (2)-(4). Thus, we can express the overall system equations as

$$\dot{x}(t) = f(x(t), F^{exc}(t), \vec{W}(t))$$

where $x(t) = [\theta(t)\ \phi(t)\ r(t)\ \dot{\theta}(t)\ \dot{\phi}(t)\ \dot{r}(t)\ x_P(t)\ y_P(t)\ z_P(t)\ \omega_{x_P}(t)\ \omega_{y_P}(t)\ \omega_{z_P}(t)\ \dot{x}_P(t)\ \dot{y}_P(t)\ \dot{z}_P(t)\ \dot{\omega}_{x_P}(t)\ \dot{\omega}_{y_P}(t)\ \dot{\omega}_{z_P}(t)]^T$ and $F^{exc}(t), \vec{W}(t)$ are exogenous inputs.

III. ANALYSIS OF KITE-PLATFORM INTERACTIONS

Using the described model, we carried out an analysis of how the platform motion affects the kite's behavior, and vice-versa. The results presented here have been obtained with the model parameters reported in Table I, corresponding to a medium-size AWES with average cycle power of 500 kW, and considering the traction phase of the pumping cycle, using the flight controller described in Section II. We estimated the AWES parameters by scaling up those of the Skysails Power SKS PN-14 reported in [1]. Regarding the buoy mass, it corresponds to a spar with diameter and height of 10 m. When no force is acting on it, the height of the platform out of the water is approximately 1 m. The ballast height is 3.6 m. The buoy centre of gravity lies on its symmetry axis, about 7 m below the deck, and its mass is about 760 tons. The numerical values of parameters M, K_h, M_∞, M_m, B_m, and K_m and the impulse response $h_{ra}(t)$ introduced in Section II-B are omitted here due to space limitations, however we made available a Matlab file containing them (where $h_{ra}(t)$ is given via a state-space realization), see [15].

Regarding the exogenous inputs, the wave excitation $F^{exc}(t)$ is described using the JONSWAP spectrum [16], characterised by three main parameters: the significant wave height H_s, the peak wave period T_e and the peak-shape parameter γ_j. We considered two sets of spectrum parameters, A and B. The set for wave A is $H_s = 0.5m$, $T_e = 3.7s$ and $\gamma_j = 3.1$, while wave B, corresponding to higher waves, has $H_s = 2m$, $T_e = 7.5s$ and $\gamma_j = 3.1$. The free surface elevation and the excitation force are computed using a random amplitude scheme, as explained in Merigaud [17]. For the wind speed $W(t)$, we considered instead a uniform wind field directed along the inertial x-axis, with magnitude equal to 8.5 m/s. We did not include a wind turbulence model in order to isolate the dynamical effects related to the wave excitation.

We first focus on the tether force behavior and compare the outcome with that of an onshore scenario.

TABLE I: Model parameters employed in the analysis

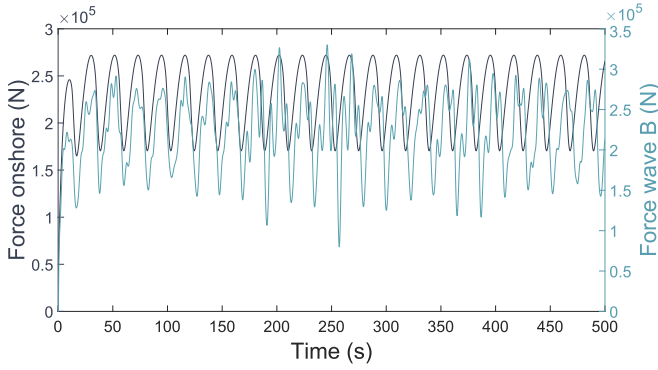|		
Kite effective area	A	360 m^2
Kite mass	m_K	90 kg
Tether diameter	d_t	0.035 m
Tether density	ρ_t	980 kg m^{-3}
Tether breaking load	$\bar{F}^{c,trc}$	950 kN
Tether breaking elongation	$\bar{\varepsilon}$	0.03
Tether exit point relative to the platform's c.o.g., in frame (x_P, y_P, z_P), when platform is at rest	$\vec{P}_{O-K}(t)$	$[0,0,7.8475]^T$
Target points	P_-, P_+	(0.6,-0.4),(0.6,0.4)

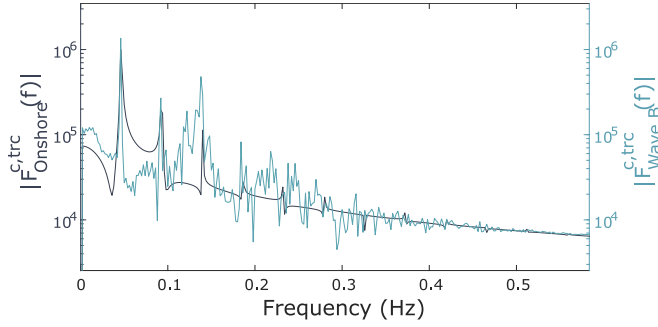Fig. 2: Comparison between onshore and offshore - wave B pulling force in N with tether length $L = 900\,\mathrm{m}$.

Fig. 3: Comparison between onshore and offshore - wave B tether force spectrum with tether length $L = 900\,\mathrm{m}$.

Fig. 3 shows the tether force spectra in onshore and offshore environment when $L = 900\,\mathrm{m}$. In the onshore case (dark blue), the spectrum contains only the frequencies pertaining to the kite's motion, while looking at wave B scenario (ligth blue), we note the presence of additional components due to the waves. We further studied the effects of waves on the tether force by evaluating its mean value, F_{mean}, the mean of its peaks, $Peaks_{mean}$, the force amplitude, ΔF, and the standard deviation of the peaks, std_{peaks} over 100 periodic patterns. Table II presents the results, reported in kN, showing that the average force is practically unaffected, while its variability and peaks change in a very limited way in case A and in a much stronger one in case B.

Next, we carried out a frequency response analysis on the platform, to assess whether the main spectral components of tether force are close to the platform's resonance peaks. Upon analyzing the Bode diagrams of the frequency response function of x_P, y_P, and z_P, we discovered that the highest resonance peaks are at $r_1 = r_2 = 0.0185\,\mathrm{Hz}$ for x_P and y_P, while for z_P, it is at $r_3 = 0.14\,\mathrm{Hz}$. The peak r_3 results to be much higher than the main frequency of oscillation of the vertical tether force, hence, we expect a limited increase and no resonance effects for the platform's heave motion. On the other hand, the resonances r_1 and r_2 are rather close to the principal components of the tether force in the x_P, y_P directions. In particular, the y component of the tether force, which has the same frequency as that of the kite's eight-path, results to be very close to the first platform resonance in the
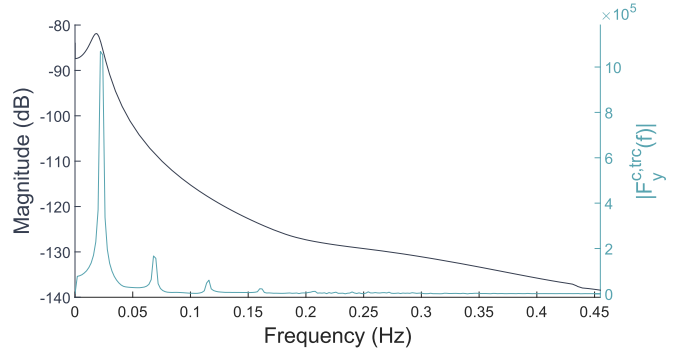

Fig. 4: Bode diagram of the frequency response of y_P w.r.t the traction force y-component, and spectrum of the latter for wave A and tether length $L = 900\,\mathrm{m}$.

sway motion. Fig. 4 highlights this correspondence showing the Bode diagram of the frequency response function of y_P with respect to the y component of the tether force vector with wave A and tether length equal to 900 m. Moreover, under the employed flight control strategy, whose switching conditions are based on the elevation and azimuth angles only, these results are affected by the tether length L. In fact, with higher L values, the length of the flown paths increases (because the angular span is the same), while the kite speed decreases, due to the higher tether drag. As a consequence, the frequency of oscillation of the tether force decreases. The overlap between the tether force spectrum and the platform resonance peaks thus depends also on L; to study this aspect for the sway motion (i.e., along the y direction) of the platform we introduce the quantity η, defined as:

$$\eta \doteq \frac{y_{P_{peak}}}{F^t_{y_{peak}}} \tag{7}$$

where $y_{P_{peak}}$ is the peak of the sway oscillation and $F^t_{y_{peak}}$ that of the tether force component along the y axis. The values of η with different tether lengths are shown in Table III, considering the case of wave A parameters: as expected by intuition, a significant increase of η is observed when the kite trajectory's frequency approaches the resonance r_2. In particular, notwithstanding a decrease of the peak force of about 33% between $L = 600\,\mathrm{m}$ and 1100 m, an increase of 230% of the platform's sway peak takes place, with a lateral movement spanning the interval $\pm 4.6\,\mathrm{m}$.

IV. PROPOSED CONTROL APPROACH

The analysis of Section III highlighted how the kite's trajectory can affect the platform oscillations, causing resonance effects which could lead to increased fatigue and damage. To avoid this problem, we propose to modify the flight control approach by adjusting the length of the flown figure-eight trajectories on the basis of the kite's velocity, in order to indirectly control the resulting frequency of the tether force oscillations. While this general idea is relevant for any trajectory planning or navigation algorithm for AWES, in the specific case of flight control strategy described in II-A it can be realized by suitably adjusting the target points' locations,

TABLE II: Comparison of the tether force values obtained in the three considered scenarios. All values in the table are in kN.

Tether length L (m)	Onshore				Offshore - wave A				Offshore - wave B			
	F_{mean}	$Peaks_{mean}$	ΔF	std_{peaks}	F_{mean}	$Peaks_{mean}$	ΔF	std_{peaks}	F_{mean}	$Peaks_{mean}$	ΔF	std_{peaks}
600	252	294	42	0.003	249	294	45	2	250	311	61	17
700	243	286	43	0.003	240	287	47	2.2	240	303	63	17
800	237	280	43	0.0009	233	281	48	2.5	233	300	77	14.7
900	228	271	43	0.002	223	273	50	2.7	224	292	78	16.4
1000	222	265	43	0.0005	216	266	50	2.13	217	287	70	15.3
1100	216	257	41	0.009	209	258	49	1.93	210	280	70	16.8
1200	206	249	43	0.1	203	250	47	1.63	203	269	76	13.8
1300	198	242	44	0.05	196	243	47	2.59	196	263	77	20

TABLE III: η values for increasing tether length in wave A scenario. f_{traj} is the frequency of the kite's figure-eight paths with the strategy described in II-A.

L (m)	f_{traj} (Hz)	$F^t_{y_{peak}}$ (kN)	$y_{P_{peak}}$ (m)	η
600	0.0324	100	2	0.02
700	0.0287	93.5	2.58	0.0276
800	0.0255	86	3.27	0.038
900	0.023	78	4	0.0513
1000	0.0208	72	4.54	0.0631
1100	0.019	67	4.6	0.0687
1200	0.0175	64	4.33	0.0677
1300	0.0161	60	3.9	0.065

P_- and P_+, as described in the remainder.
The first step is to determine a desired path frequency, f^*_{traj}, that is far from the platform resonance peaks. Then, considering the average kite's speed over one figure-eight, denoted with $\bar{v}_K$, the desired trajectory length can be computed as:

$$L^*_{traj} = \frac{\bar{v}_K}{f^*_{traj}} \qquad (8)$$

The average kite speed can be estimated from onboard measurements or, to pre-tune the approach off-line, via simulations or the simplified equations of crosswind flight, see e.g. [18]. On the other hand, with the considered switching law with two-target points, a rather accurate estimate of the trajectory length is given by:

$$L_{traj} = 2\left(\Delta\theta + \Delta\phi\right)L \qquad (9)$$

where $\Delta\theta$ is the difference between maximum and minimum θ values experienced during the flight, θ_{max} and θ_{min}, and $\Delta\phi = \phi_+ - \phi_-$, see Fig. 5 for an example. In the figure, note that the value $\theta_{min} \approx \theta_-$ can be assumed for up-loop trajectories (i.e., where the kite climbs on the sides and descends in the middle of the figure-eight), like the ones considered here. We can then estimate $\Delta\theta$ by considering the kite's turning radius R during the figure-eight patterns, typically equal to about three times the kite's wingspan, so that the distance between the highest and lowest points of each turn, denoted by Δz, is

$$\Delta z \approx 2R. \qquad (10)$$

At the same time, Δz can be also estimated in the fixed reference frame as:

$$\Delta z = L\left(\sin(\theta_{max}) - \sin(\theta_-)\right). \qquad (11)$$

Combining (10) and (11), we get $\theta_{max} = \arcsin\left(\frac{2R}{L} + \sin(\theta_-)\right)$. Using this formula, we obtain

$$\Delta\theta = \arcsin\left(\frac{2R}{L} + \sin(\theta_-)\right) - \theta_{min} \qquad (12)$$

We can finally determine the desired value of $\Delta\phi$, denoted $\Delta\phi^*$, by combining (8), (9), and (12):

$$\Delta\phi^*(t) = \frac{\bar{v}_K}{2f^*_{traj}L(t)} - \arcsin\left(\frac{2R}{L(t)} + \sin(\theta_-)\right) + \theta_{min}$$

Note that, for a fixed trajectory frequency, $\Delta\phi^*(t)$ decreases as the tether length $L(t)$ increases, as expected from the considerations reported at the end of Section III.
Then, it is sufficient to choose the target points such that $\phi_+ - \phi_- = \Delta\phi^*$ to obtain with good approximation the desired path length and frequency. For example, if the target points' positions are symmetric to the x-axis, we have $|\phi_+(t)| = |\phi_-(t)| = \frac{\Delta\phi^*(t)}{2}$. and the target points to be used are $P_- = (\theta_{min}, \phi_-(t))$ and $P_+ = (\theta_{min}, \phi_+(t))$.

V. SIMULATION RESULTS

We applied the proposed approach to control the frequency of force oscillations, and compared the results to the baseline approach of fixed target points, considered in Section II-A (target points reported in Table I). In our approach, we chose a desired oscillation frequency of $f^*_{traj} = 0.0305$ Hz, based on the analysis of Section III. Fig. 5 presents a comparison between kite patterns with old and new control approach in wave scenario B. Besides noticing the different angular width of the trajectory in the (θ, ϕ) plane, corresponding for the new approach to roughly the same linear width of 249 m in the inertial plane, the figure also highlights the slight effect of waves on the kite trajectory in scenario B.
Fig. 6 shows the spar's sway motion with $L = 1100$ m and wave A acting on the platform, with either fixed target points (baseline) or the proposed approach. Since the kite's frequency in this situation is approximately the same as the resonance ($0.019\ Hz$ and $0.0185\ Hz$), the platform moves significantly in the baseline, while the amplitude of oscillations is reduced by more than half with our method. We finally recalculated η (7) for the same tether length values and wave scenarios as those of Table III, but with the new control strategy. The outcome, displayed in Table IV, demonstrates the method's effectiveness: the tether force
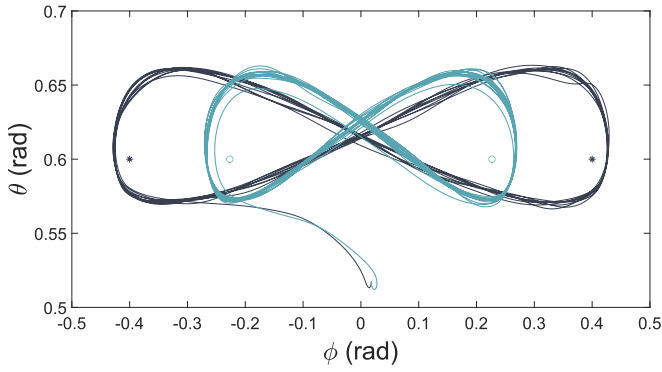
Fig. 5: Kite's path in wave B scenario, with $L = 1100\,m$. Kite trajectory and target points in the baseline approach (black lines and asterisks) and in the proposed approach to meet the desired oscillation frequency (light blue lines and circles).

Fig. 6: Platform sway motion in wave A scenario, using $L = 1100\,m$.

TABLE IV: η values with increasing tether length in wave A force scenario, using the proposed control approach

L (m)	f_{traj} (Hz)	$F^t_{y_{peak}}$ (kN)	$y_{P_{peak}}$ (m)	η
600	0.0324	100	2	0.02
700	0.0318	88	1.8	0.0205
800	0.0311	75.5	1.67	0.0221
900	0.0308	65	1.5	0.0231
1000	0.0305	58	1.35	0.0233
1100	0.0302	51	1.23	0.0241
1200	0.0298	45.5	1.13	0.0248
1300	0.0295	40.5	1.02	0.0252

oscillation frequency is kept far from the resonance, and η remains roughly constant for the whole reel-out phase.

VI. CONCLUSIONS AND FUTURE RESEARCH

The dynamical coupling between a deep offshore platform and an AWE system installed on it has been studied. The analysis and simulation results demonstrate that the wing's path may be somewhat altered depending on the wave intensity; however, such a perturbation proved to be rather limited with the waves tested. Deepening the study for more wave types would undoubtedly be of interest. Future research may also concentrate on AWES winch control techniques to attenuate the effects of waves on the tether load.

On the other hand, the analysis of the effects of the tether force on the platform motion highlighted a potential interference with the floater resonance peaks. A new control approach to keep the kite's trajectory frequency away from resonance has been presented and tested with promising results. The next steps of this research will be to investigate other platform configurations, to carry out wave tank tests for model validation, and to study an integrated kite-platform design to limit the dynamic oscillations while optimizing relevant performance indicators, such as the amount of produced energy, its cost, and the environmental footprint.

REFERENCES

[1] L. Fagiano, M. Quack, F. Bauer, L. Carnel, and E. Oland, "Autonomous airborne wind energy systems: accomplishments and challenges," *Annual Review of Control, Robotics, and Autonomous Systems*, vol. 5, pp. 603–631, 2022.
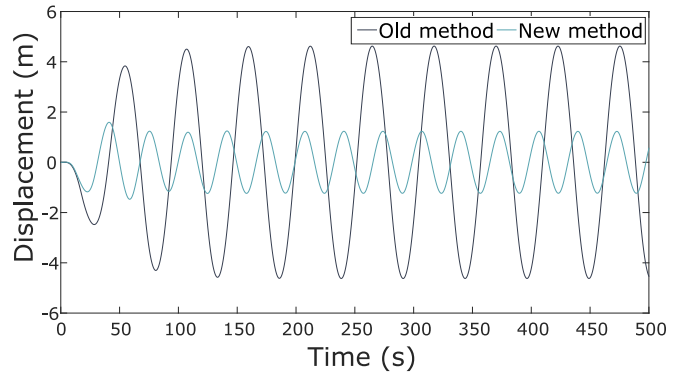
[2] P. Bechtle, M. Schelbergen, R. Schmehl, U. Zillmann, and S. Watson, "Airborne wind energy resource analysis," *Renewable Energy*, vol. 141, pp. 1103–1116, 2019.

[3] BVG Associates, "Getting airborne – the need to realise the benefits of airborne wind energy for net zero, available at https://airbornewindeurope.org," 2022.

[4] L. Fagiano, M. Milanese, and D. Piga, "High-altitude wind power generation," *IEEE Transactions on Energy Conversion*, vol. 25, no. 1, pp. 168–180, 2010.

[5] A. Cherubini, R. Vertechy, and M. Fontana, "Simplified model of offshore airborne wind energy converters," *Renewable Energy*, vol. 88, pp. 465–473, 2016.

[6] A. Cherubini, G. Moretti, and M. Fontana, *Dynamic Modeling of Floating Offshore Airborne Wind Energy Converters*, 04 2018, pp. 137–163.

[7] Makani - harnessing wind energy with kites to create renewable electricity. [Online]. Available: https://x.company/projects/makani/

[8] M. Erhard and H. Strauch, "Flight control of tethered kites in autonomous pumping cycles for airborne wind energy," *Control Engineering Practice*, vol. 40, pp. 13–26, 2015.

[9] M. Canale, L. Fagiano, and M. Milanese, "High altitude wind energy generation using controlled power kites," *IEEE Transactions on Control Systems Technology*, vol. 18, no. 2, pp. 279–293, 2010.

[10] L. Fagiano, A. U. Zgraggen, M. Morari, and M. Khammash, "Automatic crosswind flight of tethered wings for airborne wind energy: Modeling, control design, and experimental results," *IEEE Transactions on Control Systems Technology*, vol. 22, no. 4, pp. 1433–1447, 2014.

[11] P. G. Drazin and N. Riley, *The Navier-Stokes Equations: A Classification of Flows and Exact Solutions*, ser. London Mathematical Society Lecture Note Series. Cambridge University Press, 2006.

[12] W. Cummins, *The Impulse Response Function and Ship Motions*, ser. Report (David W. Taylor Model Basin). Department of the Navy, David Taylor Model Basin, 1962.

[13] N. Faedo, "Optimal control and model reduction for wave energy systems: A moment-based approach," Ph.D. dissertation, Maynooth University, Irland, 2020.

[14] A. Babarit and G. Delhommeau, "Theoretical and numerical aspects of the open source BEM solver NEMOH," in *11th European Wave and Tidal Energy Conference (EWTEC2015)*, Nantes, France, Sep. 2015.

[15] S. Trombini. (2023) Offshore platform parameters. [Online]. Available: http://www.sas-b.deib.polimi.it/wp-content/uploads/2023/11/Offshore_platform_parameters.zip

[16] K. Hasselmann, "Measurements of wind-wave growth and swell decay during the joint north sea wave project (jonswap)," *Deut. Hydrogr. Z.*, vol. 8, pp. 1–95, 1973.

[17] A. Merigaud and J. Ringwood, "Free-surface time-series generation for wave energy applications," *IEEE Journal of Oceanic Engineering*, vol. PP, pp. 1–17, 04 2017.

[18] L. Fagiano, M. Milanese, and D. Piga, "Optimization of airborne wind energy generators," *International Journal of Robust and Nonlinear Control*, vol. 22, no. 18, pp. 2055–2083, 2012.